Transient Modeling of Hybrid Rocket Low Frequency Instabilities

M. Arif Karabeyoglu*, Shane De Zilwa†, Brian Cantwell‡ and Greg Zilliac§

Abstract

A comprehensive dynamic model of a hybrid rocket has been developed in order to understand and predict the transient behavior including instabilities. A linearized version of the transient model predicted the low-frequency chamber pressure oscillations that are commonly observed in hybrids. The source of the instabilities is based on a complex coupling of thermal transients in the solid fuel, wall heat transfer blocking due to fuel regression rate and the transients in the boundary layer that forms on the fuel surface. The oscillation frequencies predicted by the linearized theory are in very good agreement with 43 motor test results obtained from the hybrid propulsion literature. The motor test results used in the comparison cover a very wide spectrum of parameters including: 1) four separate research and development programs, 2) three different oxidizers (LOX, GOX, N_2O), 3) a wide range of motor dimensions (i.e. from 5 inch diameter to 72 inch diameter) and operating conditions and 4) several fuel formulations. A simple universal scaling formula for the frequency of the primary oscillation mode is suggested.

1) Nomenclature:

A:	Pre-exponential coefficient
A_p, A_n:	Port and nozzle throat areas
B:	Blowing parameter
C:	Specific heat of fuel
c^*:	Boundary layer delay time coefficient
C_f, C_H:	Skin friction coefficient and Stanton number
c^*_{exp}, c^*_{theo}:	Measured and calculated characteristic velocities
$\overline{D}$:	Average port diameter
E_a:	Activation energy
E_L, E_{E_a}:	Energy Parameters
f, f_{1-L}:	Primary oscillation frequency, first acoustic mode frequency
F_T:	Thermal system transfer function
F_{TC}:	Thermal-Combustion coupled system transfer function
G_o, G_t:	Oxidizer and total mass fluxes
h_v, L_v:	Total and latent heats of gasification
k:	Blowing parameter exponent
$\hat{J}$:	Laplace transform of oxidizer mass flux perturbation
L, L_m:	Length of the fuel port and motor
L^*:	V_m/A_n
$\dot{m}_o$, $\dot{m}_t$:	Oxidizer and total mass flow rate
n:	Mass flux exponent
O/F:	Oxidizer to fuel ratio
P_c:	Average chamber pressure
$\dot{Q}_c$, $\dot{Q}_w$:	Convective and total wall heat fluxes
$\dot{r}$, $\bar{R}$:	Dimensional and non-dimensional regression rate
Re_z:	Reynolds number
R_g R_u:	Specific and universal gas constants
RT_{avg}:	Average gas constant temperature product
s:	Laplace transform variable
t:	Time
T:	Temperature
u, v:	Axial and normal velocities
U^*:	Diffusion speed

* Research Associate, Dept. of Aeronautics and Astronautics, Stanford University, Member AIAA
† NRC Post Doctoral Fellow, NASA Ames Research Center, Member AIAA
‡ Professor, Dept. of Aeronautics and Astronautics, Stanford University, Fellow AIAA
§ Research Scientist, NASA Ames Research Center, Member AIAA

V_p, V_m:	Port and motor volumes
z:	Axial distance along the port
δ:	Boundary layer thickness
ΔP_{osc}:	Chamber pressure oscillation amplitude
γ:	Ratio of specific heats
κ:	Thermal diffusivity of fuel
ρ_f, ρ:	Fuel and average gas densities
τ_H, τ_d:	Boundary layer response time and thermal lag time
τ_w:	Shear stress
σ_1, σ_2:	Gas phase response coefficients
μ:	Average gas viscosity
Subscripts:	
a:	Ambient
1:	First perturbation variable
e:	Free stream value
ref:	Reference quantities
s:	Surface
Superscripts:	
-	Non-dimensional variable
^:	Laplace transform variable

2) Introduction:

The allowable thrust oscillations for an operational propulsion system are limited by certain practical considerations including acceleration loads on the vehicle structures and also on the payload. This makes combustion stability a critical issue during the development of a new propulsion system. The combustion instabilities of solid and liquid systems have been studied in depth and partially successful theories along with certain practical rules for designing stable systems have been developed[1,2,3]. Even with this extensive knowledge base, development of stable rocket systems requires significant amount of time and resources during the design and testing phases of a new system. Even though the transient operation and instability mechanisms of hybrids have not been explored as extensively as the more mature chemical systems, past experience shows that hybrids do not have the catastrophic instabilities that liquid and solid systems may potentially present.

In fact, hybrid systems typically show finite amplitude (i.e. 2-20% rms of mean chamber pressure) low-frequency chamber pressure oscillations[4,5,6,7,8]. This most common hybrid instability is in the form of limit cycle oscillations with frequencies much smaller than the first longitudinal acoustic mode of the combustion chamber.

Even though the exact cause of the low frequency hybrid instabilities is not yet known, a few plausible theories exist[5,9,10,11,12]. Most of the suggested theories lack the mathematical formalism that exists in the solid and liquid instability models. The fundamental difficulty in producing a mechanism that would generate instabilities comes from the fact that hybrid burn rates are typically independent of the chamber pressure. This, for example, eliminates the pressure coupling between the thermal lags in the solid and the chamber gas dynamics which is the source of the L* instabilities in solid rockets[1].

One particular theory, the TC coupled model[13,14], which is based on the coupling of thermal lags in the solid and the lags in the gas phase transport, has predicted (based on a mathematical formalism) fuel mass production oscillations that would drive the observed pressure oscillations. The purpose of this paper is to extend the TC coupled theory to include the effects of the *chamber* gas dynamics and compare the theory predictions with the motor test data. The merits and shortcomings of the TC coupled model will also be discussed.

3) Transient Phenomena in Hybrid Rocket Motors:

Our approach to modeling the dynamic behavior of hybrids is to isolate the subsystems of the motor and consider every single subsystem individually. For a full description of motor transients one has to consider the following subsystems.

a) Feed System: In a hybrid motor, the liquid (or gaseous) oxidizer needs to be fed in to the combustion chamber through a feed system. In reality the feed system response time is finite due to the capacity of the elements in the system. Accurate response depends on the details of the system, which is likely to be significantly different for every design. For this reason we will bypass the feed system dynamics in our investigations by assuming the oxidizer mass flow rate as the input parameter. This is a reasonable assumption for most systems because isolating elements (i.e. cavitating venture, sonic orifice) are present.

b) Vaporization of the Liquid Oxidizer: Complete vaporization of the oxidizer droplets in

the combustion chamber requires a certain characteristic time depending on parameters such as the droplet size and the thermal/flow environment of the space where droplet vaporization takes place. For the purposes of this paper we will assume that the oxidizer is in gaseous phase when it enters the port.

c) Diffusion and Combustion in the Boundary Layer: It requires some time for the hybrid boundary layer properties to adjust to the changes in the port velocity or the fuel blowing from the surface. The associated dynamics has been discussed in detail in Refs. 13, 14 and will be briefly covered in section 5 of this paper.

d) Thermal Response in the Solid Grain: A change in the wall heat flux to the hybrid fuel grain can not be followed immediately by fuel production due to the finite heat capacity of the solid fuel.

e) Chamber Gas Dynamics: The chamber pressure responds to the changes in the mass flow with a time scale proportional to the filling time of the chamber. Acoustic response is also resolved in this sub-system.

In the subsequent sections the last three of these sub-systems (sections c-e) will be modeled and investigated individually. Eventually, these subsystems will be coupled to give the overall system response. The order of magnitude estimates of the time scales of some of the important processes encountered in a typical hybrid motor are listed in Table 1. In our modeling, solid and gaseous kinetic times are assumed to be fast compared to the other relevant time scales.

4) Thermal Lag Model:

The regression rate of the hybrid fuel grain cannot respond to the changes in the surface heat flux instantaneously due to the finite thermal conductivity of the solid fuel. A complete transient model for a hybrid rocket system requires a dynamic model to predict the regression rate history for a given wall heat flux schedule. In order to serve this purpose a thermal lag model that models the nonlinear heat conduction in the fuel grain with a moving boundary has been formulated and reported in Refs.13 and 14. The schematic of this particular model is shown in Figure 1.

In the thermal lag model, the gasification and pyrolysis reactions at the surface are both modeled by an exponential expression of the Arrhenius type. For chemical reactions, the exponential constant is an activation energy, whereas in vaporization it is the latent heat. In order to describe this behavior, we assign an average effective activation energy, E_a, resulting in:

$$\dot{r} = A\, e^{-E_a/R_u T_s} \tag{1}$$

Here T_s is the surface temperature, $\dot{r}$ is the regression rate and R_u is the universal gas constant. The mathematical formulation and various solution techniques for the thermal lag model are presented in Ref 13. One solution of interest is obtained by perturbing the full nonlinear system around the nominal operating point. The linear initial-boundary value problem defined for the first order perturbation quantities has been solved with use of the Laplace transformation technique. The transfer function between the regression rate perturbation and the applied heat flux perturbation can be written as

$$F_T = \frac{\hat{R}_1(s)}{\hat{Q}_1(s)} = \frac{2E_{E_a} s}{\left(1+\sqrt{4s+1}\right)\left(s+E_{E_a}\right) - 2E_{E_a} + 2E_L E_{E_a} s}. \tag{2}$$

Note that $\hat{R}_1(s)$ and $\hat{Q}_1(s)$ are the Laplace transforms of the non-dimensional regression rate perturbation and the wall heat flux perturbation, respectively. Here the following non-dimensional parameters are defined for convenience.

$$E_{E_a} = \frac{E_a \Delta T}{R_u (T_s)_{ref}^2} \qquad E_L = \frac{L_v}{C\Delta T}$$

$$\Delta T = (T_s)_{ref} - T_o \qquad \overline{Q} = \frac{\dot{Q}_w}{\dot{Q}_{ref}}$$

$$R = \dot{r}/\dot{r}_{ref} \quad \dot{Q}_{ref} = \dot{r}_{ref}\rho_f C\Delta T$$

The reference-state indicated by subscript "ref" corresponds to the nominal operating point around which the system is perturbed.

Equation 2 relates the wall heat flux to the regression rate in the Laplace space and establishes one block in our overall transient model that is shown schematically in Figure 2. Various important characteristics of a linear system including stability can be inferred from the denominator of its transfer function commonly referred as the characteristic equation. This transfer function for the thermal system, which contains a square root term, produces a phase lead between the heat flux and the regression rate in the low end of the frequency domain[13]. As it will be discussed in the following sections, this phase lead capability will play a critical role in the production of low frequency instabilities.

5) Gas Phase Combustion Model:

In the thermal lag model we have treated the surface heat flux as a parameter that can directly be controlled. However, in a hybrid motor, the oxidizer mass flow rate is the primary input variable that can be controlled directly. The actual response of the motor to a change in the oxidizer mass flow is rather complicated during a transient. As the oxidizer mass flow rate of the motor changes, the mass flux at a characteristic point in the port reacts to the change as does the turbulent boundary layer developed over the fuel surface. In this section we will summarize the modeling of the boundary layer combustion dynamics and investigate its interactions with the thermal lags in the solid. For the sake of simplicity, we will ignore the radiative heat transfer to the fuel surface, which is typically a relatively small fraction of the total heat flux. Unless the radiation dominates the convection component of the surface heat transfer, the transient model developed in this paper is expected to be valid.

In our preliminary model we assume that the boundary-layer response is quasi-steady, namely the boundary-layer diffusion lag times are small compared to the thermal lag times in the solid. Under the quasi-steady assumption one can use the classical approach[15] to calculate the response of the wall heat flux to the changes in mass flux. However, the results of classical hybrid theory cannot be used directly during a transient in the solid, due to the fact that the convective heat transfer to the wall depends explicitly on the instantaneous regression rate through the blocking generated by the blowing of the gaseous fuel from the surface. In the presence of the thermal lags, the blocking generates a coupling mechanism in the gas phase between the regression rate and the heat flow to the surface. Based on this understanding, the classical theory can be modified to obtain a functional relation between wall heat flux and oxidizer mass flux-regression rate combination in terms of non-dimensional parameters:

$$\overline{\dot{Q}}_c(\bar{t}) = E_L \overline{G}_o^{n/(1-k)} R^{-k/(1-k)} \qquad (3)$$

Note that $\overline{G}_o = G_o/(G_o)_{ref}$, $\overline{\dot{Q}}_c = \dot{Q}_c/\dot{Q}_{ref}$ and n is the oxidizer flux exponent, k is the blowing correction exponent first defined by Marxman (i.e. $C_H/C_{Ho} = B^k$). Here the local total mass flux that appears in the original Marxman formulation is replaced by the oxidizer mass flux for convenience. The justification for that transformation is given in Ref. 14.

Thus far in the development of the transient hybrid combustion theory we assumed that the boundary layer responds rapidly to the changes in the mass flux compared to the other transient time scales in the rocket motor such as the gas dynamic lags or the thermal lags. This assumption fails to be valid especially for large hybrid motors. In order to develop a realistic model for the dynamics of the hybrid motor, the boundary layer lags must be considered. Since this complex dynamic phenomenon is extremely difficult to investigate both theoretically and experimentally, we consider the simpler cases reported in the literature of an incompressible turbulent boundary layer with no blowing or chemical reactions[16]. The most important conclusion for this simplified case is that the time required for transition from the initial equilibrium profile to the final equilibrium profile at any axial location, z, is proportional to the time of flight of a fluid particle from the leading edge of the boundary layer to the specific axial location at the speed of the free stream flow, u_e. This very important result can be formulated for hybrid boundary layers as

$$\tau_{bl} = c' \frac{z}{u_e}. \qquad (4)$$

Here c' is a constant that needs to be determined empirically. We will call this time required for equilibration, the characteristic response time of the boundary layer, τ_{bl}. It is

important to note that the physical nature of the boundary layer transient time is not related to the propagation of the disturbances with the speed of the port velocity as suggested by Equation 4. The delay rather depends on the diffusion time scale across the boundary layer which is proportional to the ratio of the local boundary layer thickness to the diffusion speed, $\tau_{bl} \cong \delta/U^*$. The diffusion speed is defined in terms of the shear stress and mean gas density as $U^* = \sqrt{\tau_o/\rho}$. The boundary layer delay time, after the substitution of the standard (incompressible) turbulent boundary layer expressions[17] for the shear stress, $\tau_o = 0.0288\rho\, u_e\, \mathrm{Re}_z^{-0.2}$, and the thickness, $\delta = 0.37z\,\mathrm{Re}_z^{-0.2}$, becomes $\tau_{bl} = 2.18\,\mathrm{Re}_z^{-0.1}\, z/u_e$. Here the local Reynolds number is defined as $\mathrm{Re}_z = u_e z\rho/\mu$. Note that the coefficient c' is found to be a weak function of the local Reynolds number. Thus, for simplicity, we assume that c' is constant. For Reynolds numbers corresponding to typical hybrid operation, c' is estimated to be approximately 0.55. In a real hybrid boundary layer with combustion and blowing, c' can be different from this estimation and for that reason, it is determined empirically.

For the purpose of this paper, it is convenient to consider an average boundary layer delay and replace the local distance z, with the half of the grain length, $L/2$. Note that the empirical constant c' accounts for the correction to the inaccurate selection of the length scale, L. However, we recognize that in reality there is a range of boundary layer delay times that should be considered. Thus the significant observation here is that a relatively broad band of oscillation frequencies is expected as opposed to a very sharp peak at the center frequency corresponding to $L/2$.

In our studies the response of the boundary layer to the changes in the mass flux is accounted for by simply inserting time delays in the heat-flux expressions derived under the assumption of quasi-steady response. The implementation of this idea in the linearized version of Eq. 3 yields

$$\overline{Q}_1(\bar{t}) = \sigma_2 \overline{G}_1(\bar{t} - \bar{\tau}_{bl1}) - \sigma_1 R_1(\bar{t} - \bar{\tau}_{bl2}) \qquad (5)$$

where

$$\bar{t} = t/\tau_{il}\,,\quad \bar{\tau}_{bl1} = \tau_{bl1}/\tau_{il}\,,\quad \bar{\tau}_{bl2} = \tau_{bl2}/\tau_{il}$$

$$\sigma_1 = (E_L + 1)\left(\frac{k}{1-k}\right),\ \sigma_2 = (E_L + 1)\left(\frac{n}{1-k}\right)$$

and $\tau_{il} = \kappa/\dot{r}^2$.

Here τ_{bl1} and τ_{bl2} are the time delays experienced by the wall heat flux ($\dot{Q}_c$) to the changes in the oxidizer mass flux and the regression rate, respectively. The scaling of the time delays τ_{bl1} and τ_{bl2} obey the general scaling law given by Eq. 4. However the c' coefficients for τ_{bl1} and τ_{bl2} are expected to be different since each of these delays represents a different adjustment mechanism for the boundary layer. The model presented by Equation 5 is central to the analysis in that it relates the heat conduction in the solid to the boundary layer combustion.

6) Thermal-Combustion (TC) Coupled System

Now, with the use of Equation 5 the thermal lags in the solid can be coupled to the combustion transients in the boundary layer. This coupling yields the following transfer function between the oxidizer mass flux ($\hat{I}(s)$) and the regression rate ($\hat{R}_1(s)$) and represent the Hybrid Combustion block in the overall transient model (Figure 2).

$$F_{TC}(s) = \frac{\hat{R}_1(s)}{\hat{I}(s)} = \frac{2E_{E_a}\sigma_2 e^{-\bar{\tau}_{bl1}s}\, s}{\left(1+\sqrt{1+4s}\right)\left(s+E_{E_a}\right) - 2E_{E_a} + 2E_{E_a}\, s\left(E_L + \sigma_1 e^{-\bar{\tau}_{bl2}s}\right)}. \qquad (6)$$

This transfer function (TC coupled system) that represents the combustion phenomenon includes the dynamics of the thermal processes in the solid and approximates the combustion dynamics in the turbulent boundary layer of the rocket motor. Equation 6 can be used

to investigate the stability character of the TC coupled system. The commonly used method is to map the poles of the transfer function in the s-plane. Particularly, the real component of a certain pole of a transfer function indicates amplification rate associated with that pole. Similarly the imaginary part represents the oscillation frequency.

First a system with zero boundary layer delays (i.e. $\tau_{M1} = \tau_{M2} = 0$ is determined to be always stable. In fact plot of the transfer function for a system with typical parameters shows no poles in the s plane (only a zero at (0, 0)) indicating no sign of instability (i.e. See Figure 3). If a positive delay is introduced between the regression rate and wall heat flux, a series of unstable poles is generated. The example case with a 38 msec delay is shown in Figure 4. Note that all the other parameters are kept identical to the case with no delays. Even though there exists an infinite series of poles generated (at the same amplification rate) we will only concentrate on the pole with the lowest frequency (fundamental mode). We believe that the higher order modes are an artifact of using a simple delay instead of the full dynamics for the boundary layer transients. Moreover the higher frequency modes, even if they exist in a real system, are likely to be damped more effectively compared to the fundamental mode.

It is important to identify the necessary conditions that must exist for the generation of TC coupled instabilities. A careful examination of the denominator of the transfer function, Eq. 6, shows that for the instability to exist blowing exponent, k, activation energy, E_a and delay time, τ_{M2} must be nonzero. This indicates that the instability is a result of the coupling of three physical phenomena: blocking of heat transfer by radial injection of fuel mass, thermal transients in the solid and boundary layer dynamics. The gas phase/solid phase coupling mechanism captured by the TC coupled model is shown in Figure 1.

Next we consider the effect of various parameters on the TC coupled instability. It can be shown that the effect of the regression rate mass flux exponent n, heat of vaporization of the fuel, L_v, the heat capacity of the solid fuel, C, and the surface temperature, T_s, on the oscillation frequency and amplitude are negligible for the range of these parameters that are commonly found in hybrid systems. Also TC coupled system characteristics are completely independent of the solid density, ρ_f and the heat diffusivity in the solid, κ.

The effect of the activation energy on the amplification and frequency is shown in Figure 5 for τ_{M2}=38 milliseconds and k=0.68. As indicated by the figure, for activation energies commonly observed in hybrids, ranging from 5 kcal/mole to 60 kcal/mole, the variation in the oscillation frequency is relatively small. The amplification increases with increasing activation energy. For this specific case the systems with activation energies larger than 3 kcal/mole show positive amplification and unstable behavior. Decreased stability at higher activation energies is expected since at high E_a values the surface temperature and regression rate are more closely coupled. This coupling is one of the necessary ingredients for the generation of the instabilities. In fact in the extreme case of E_a=0, for which the surface temperature is completely independent of the regression rate, oscillation frequency goes to infinity and the amplification goes to negative infinity.

The activation energies for the polymeric systems that are typically used in hybrids ranges from 10 kcal/mole to 60 kcal/mole. For the nonpolymeric paraffin-based fuel system the activation energy is equivalent to the latent heat of vaporization[18]. This value for the paraffin-based fuel formulations is estimated to be 17 kcal/mole (Ref. 13).

Similar results can be obtained for the effect of the blocking exponent, as shown in Figure 6 for τ_{M2}=0.38 and E_a=15 kcal/mole. For the range of values reported in the literature for k (i.e. 0.68-0.77)[15,19], the effect of blowing exponent on the frequency is negligible. The amplification increases with increasing k and systems with k values 0.45 and larger showed unstable behavior. Note that for the physically unrealizable case of k=0 the instability disappears, since one of the necessary coupling mechanisms is eliminated. We finally like to note that even though the blocking effect in paraffin based systems is somewhat reduced due to the two phase character of the flow field, its is still significant enough to establish the coupling between the gas phase and solid phase.

The most influential parameter on the TC coupled frequency is determined to be the boundary delay time, τ_{M2}. Figure 7 shows the

predicted frequency as function of the delay time for three activation energy values, E_a=5, 15 and 50 kcal/mole. As shown in the figure, the effect of the activation energy on the frequency, especially at longer delay times, is small. For the purposes of this paper the effects of activation energy and blowing exponent will be ignored and the frequency will be represented as a function of the boundary delay time alone. The following curve fit equation is suggested to quantify the inverse relationship between the frequency and the boundary layer delay time.

$$f = \frac{0.48}{\tau_{M2}} \qquad (7)$$

As shown in Figure 7, this expression represents the predicted frequency to a very high degree of accuracy and will be used for all the hybrid systems that will be discussed later in this paper.

7) Gas Dynamic Model:

In the previous section the dynamic models for the thermal lags and the hybrid combustion are summarized. In addition, these subsystem models are coupled to obtain the response of the fuel mass generation to the changes in the mass flux in the port. However, practically significant parameters of the rocket operation such as the chamber pressure, specific impulse and thrust cannot be obtained solely from the TC coupled system. These variables can only be determined after introducing a model for the gas dynamics which will be discussed in this section. A gas dynamic model, in general, should use the oxidizer mass flow rate and the fuel mass generation rate as the inputs and it should yield the parameters that are more closely related to the performance of the motor such as the chamber pressure and the motor O/F ratio as the outputs.

In our specific model (2V-port model) we divide the chamber into three components, pre-combustion chamber, port volume and the post-combustion chamber (i.e. see Figure 8). We treat the pre and post combustion chambers as zero dimensional volume elements, but consider the variation of state variables along the axis of the port. The mathematical formulation is obtained after the application of the conservation laws for the three volume elements. The set of equations resembling our model is solved analytically after linearization and as a result of that operation, a transfer function for the gas dynamic subsystem is obtained. Some numerical simulations are also performed to determine the validity of the approximations used in the perturbation solutions. Note that a detailed description of the gas dynamic model is given in the Appendix of this paper.

The following conclusions can be drawn from the results of the gas dynamic model as given in detail in the Appendix of this paper and in more detail in Ref. 13.

- Gas dynamic model captures the filling/emptying dynamics and also the longitudinal acoustic response of the hybrid combustion chamber. As can be seen from Figure 13 acoustic modes are stable (well damped). No unstable oscillation modes are generated by the gas dynamic system by itself.
- The nonlinear disturbances excite the chamber acoustic modes. Simulations showed that a sudden pulse in the oxidizer mass flow rate excites the acoustics modes. These modes decay in a relatively short period. This ringing phenomenon shows that the longitudinal acoustic modes can be driven by nonlinear low frequency oscillations. Namely the nonlinear low frequency pressure waveforms continuously excite the acoustic modes of the chamber. AMROC motor DM-01 showed at least 5 longitudinal acoustics modes. All those were well damped. The gas dynamic model when corrected for isentropic speed of sound predicts the acoustics frequencies of the DM-01 motor to a high level of accuracy (See Table 7).
- Gas dynamic model coupled with the boundary layer dynamics ($\tau_{M1} \neq 0$) does not produce any instabilities (no extra poles are generated in the s plane). This conclusion is based on transfer function analysis and also numerical simulations. This important result highlights the importance of the thermal lag system (i.e. and its unique dynamic capability of producing a phase lead) in producing a coupling mechanism to generate low frequency unstable modes.

8) Thermal-Combustion-Gas dynamic (TCG) Coupled System:

In this section we integrate the gas dynamic system to the TC coupled system to establish the TCG coupled response (i.e. See Figure 2). The TCG coupled system yields the performance of the rocket (such as chamber

pressure) for some given input of oxidizer mass flow rate, which is a fundamental control parameter in hybrid rockets. It is fair to state that the TCG coupled system represents the most fundamental dynamic behavior of a hybrid rocket.

The schematic of the hybrid subsystems and the information flow between the subsystems in the context of TCG coupling are shown in Figure 2. Note that the lower block in the schematic represents the TC coupled system. The input for the TC coupled system is the local mass flux information and the output is the mass generation or the regression rate. The upper block shows the 2V-port gas dynamic model. The gas dynamic model takes the oxidizer flow rate and the mass generation rate information and reveals the important performance parameters such as the chamber pressure and specific impulse. The TCG coupled system can be considered as an overall model for the dynamics of a hybrid propulsion system that utilizes gaseous oxidizer which is delivered by an isolated feed system.

The generalization of the TCG coupled system to a liquid hybrid with significant feed system dynamics can be achieved easily. Namely two more modules for the liquid droplet evaporation and the feed system dynamics must be added to the front end of the TCG model. We believe that the fundamental phenomenon generating the low frequency instabilities of hybrid systems does not involve either of the evaporation lags or the feed system dynamics.

In the TCG coupled system the gas dynamic module converts the fuel mass oscillations produced by the TC coupled system into the chamber pressure oscillations. It has been determined that in the process of conversion, the oscillations produced by the TC coupled system (i.e. frequencies and amplification rates) are not altered. This fact is demonstrated in Figure 9, which shows a plot of the TCG system transfer function for the TC coupled system depicted in Figure 4. The same plot also indicates poles associated with the filling/emptying mode (first order non-oscillatory mode) and the longitudinal acoustic modes with negative real components (damped). TCG coupled system captures all the necessary underlying dynamics (linearized version) of a gaseous hybrid with a decoupled feed system.

9) NASA Ames Paraffin-Based Motor Tests:

A promising fast burning paraffin-based fuel has been tested extensively in the Hybrid Combustion Facility (HCF) at NASA Ames[20]. The motor outside diameter is 10 inches and gaseous oxygen is the oxidizer for all the tests conducted at the HCF. The pressure time trace of a typical paraffin-based hybrid motor test is shown in Figure 10, whereas the Fourier transform for the same test is given in Figure 11. Note that the chamber pressure traces for classical hybrids as presented in the literature are very similar in nature. As indicated in Figure 10 for a particular case, the feed system and the chamber were completely decoupled for all paraffin-based motor tests used in this paper.

The Fourier transform shows three broad peaks corresponding to the low frequency hybrid instability, the Helmholtz mode and the first longitudinal mode. It has been generally observed that the dominant mode, low frequency oscillations are accompanied by lower amplitude higher frequency acoustic modes. See Ref. 6 for an extensive discussion of the stability characteristics of the paraffin-based motors.

10) Comparison of Theory Results with the Motor Test Data

In this section we will compare the TC coupled theory oscillation frequency predictions with the chamber pressure oscillation frequencies from hybrid motor test data. In order to produce a conclusive comparison, we have selected a large number of tests form several hybrid rocket development programs. The key features of each program is discussed briefly in the following paragraphs.

- AMROC Motor Tests[4,13]: In this case the reported results are for 4 different thrust class hybrid motors which all utilized LOX/GOX as the oxidizer and HTPB as the fuel. The data from the AMROC tests is given in Table 2.
- HPDP 11 Inch Motor Tests[5,8]: The oxidizer used in these tests is LOX and GOX and the fuel is HTPB/Escorez formulation. The motor case diameter was 11 inches and the data from 5 tests used in this study is given in Table 3. Only the tests that exhibit combustion instability and performed with single port motors are considered. The runs with the rearward-facing steps at the port entrance are also excluded in this study, since in these tests

the flow field in the port is significantly altered which may cause a major change in the boundary layer delay time coefficient. We also include test #1 of 11 inch LOX motor data in the analysis. We only consider test 1 since it is the only run with a chamber configuration identical to GOX motors used in the calculations.

- JIRAD Motor Tests[13,21]: The oxidizer used in these tests is GOX and the fuel is HTPB/Escorez formulation. The motor case diameter was 11 inches and the data from 8 tests used in this study is given in Table 4. Only the tests that exhibit combustion instability and performed with single port motors are considered here.
- Arizona State University[22]: One test is included in the comparison for a 5 inch diameter nitrous oxide motor. The fuel was HTPB (i.e. See Table 5).
- Paraffin-Based Motor Tests[29]: These tests are conducted at NASA Ames in a 10 inch diameter test facility. The oxidizer was GOX and the fuel is two separate nonpolymeric paraffin-based formulations (SP-1a and SP-4). The data form 25 motor tests are reported in Table 6.

The prediction of the frequency requires the estimation of the boundary layer delay time for each test from the reported data. Since the reported data is somewhat different for each program different scaling laws for the delay time must be derived.

The first one of those is for the various size AMROC motors which operated at different L^* levels. Since the information on the AMROC motors that can be found in the literature is limited to L^*, c^* and motor O/F ratio, it is desirable to express the boundary layer delay time, Equation 4 (with $z = L/2$) in terms of those variables. The average velocity in the port can be approximated as

$$u_{ave} = \frac{G_t\left[(1+2O/F)/(1+O/F)\right]RT_{ave}}{2P_c}. \qquad (8)$$

where RT_{ave} is an average value in the port. Substituting this expression in the delay formula and using the relations for the total mass flow rate $\dot{m}_t = G_t A_p$ and port volume $V_p = LA_p$ yields

$$\tau_{bl2} = c'\frac{V_p P_c}{\dot{m}_t\left[(1+2O/F)/(1+O/F)\right]RT_{ave}}. \qquad (9)$$

With the use of the total mass flow relation, $\dot{m}_t = P_c A_n / c^*_{exp}$ and the definition $L^* = V_m / A_n$, the delay equation can be written as

$$\tau_{bl2} = c'\frac{V_p}{V_m}\frac{\left[(1+O/F)/(1+2O/F)\right]}{RT_{ave}}L^* c^*_{exp}. \qquad (10)$$

Here V_p/V_m is the ratio of the port volume to the motor volume, which is estimated to be approximately 0.8 for AMROC DM-01 motor. We assume that all AMROC motors possess the same average gas constant temperature product, RT_{ave} and volume ratio, V_p/V_m. After noting that all motors operate at very similar O/F ratios and c^*_{exp} values, it can be stated that in the series of tests the boundary layer characteristic delay time is proportional to L^*.

In order to reduce data form the rest of the tests, a similar relation for the boundary layer delay time in terms of the chamber pressure and port flux levels must be derived. The port velocity can be replaced by an average value $(G_o + G_t)/2\rho_{ave}$ with ρ_{ave} given by the gas law $P_c = \rho_{ave} RT_{ave}$ to yield finally for the boundary layer lag:

$$\tau_{bl2} = c'\frac{LP_c}{(G_o + G_t)RT_{ave}} \qquad (11)$$

Equation 11 gives the scaling law for the boundary layer delay in terms of the operating points of the rocket motor and also with the size of the motor. This states that delay increases with increasing chamber pressure, port length and decreases with increasing mass flux in the port. An important conclusion that can be drawn from those observations is that an increase in the chamber pressure or a decrease in the port mass flux act to decrease the oscillation frequency of this type of TC coupled system.

The total mass flux can be eliminated form Equation 11 by introducing the average oxidizer to fuel ratio of the motor.

$$\tau_{bl2} = c'\frac{LP_c}{\left(2+\frac{1}{O/F}\right)G_o RT_{ave}} \qquad (12)$$

Equation 12 will be used to reduce the paraffin-based motor data.

Note that equations 10, 11 and 12 are equivalent and the constant multiplier c' is identical for all of these expressions.

The average temperature gas constant product that appears in the denominator of all the boundary layer delay time equations is assumed to be constant for all of the LOX/GOX motor tests that is considered in this paper. This is a fairly good assumption since RT is a weak function of the motor O/F for the practical operating conditions[13]. In fact the maximum expected variation on the RT values for all the LOX/GOX tests used for comparison is predicted to be less than 5%. The absolute value of RT_{ave} is selected to be 6.39 10^5 (m/sec)^2 for LOX/GOX motor tests and since the same value is used for all calculations any error in RT_{ave} will only effect the numerical value of the empirical delay constant c'.

In order to double check the RT_{ave} value used in the calculations one could use the first acoustic frequency measured form the motor test data and use that to estimate the speed of sound and finally RT_{ave} based on the following equation.

$$f_{1-L} = \frac{\sqrt{\gamma\, RT_{ave}}}{2L_m} \qquad (13)$$

Here γ is the ratio of the specific heats averaged over the length of the motor, f_{1-L} is the first longitudinal acoustic mode and L_m is the effective length of the motor. For a more accurate calculation the complex gas dynamic model discussed in the Appendix of this paper can be used. All of the NASA Ames motor tests with 45 inch long grains had their first acoustic mode at around 370 Hz. For these tests with use of γ=1.25 and L_m=1.27 m, one obtains RT_{ave} of 7.1 10^5 (m/sec)^2 which is only 10% higher than the assumed value. RT_{ave} for the N_2O test is selected to be 5.1 10^5 (m/sec)^2. This is 20% lower than the RT_{ave} for the GOX/LOX system due to the low temperature of the N_2O/hydrocarbon combustion products.

Now Equation 7 can be coupled with the expressions for the boundary delays time to evaluate the frequencies predicted by the TC coupled model.

$$f = 0.48\frac{RT_{ave}}{c'\left(V_p/V_m\right)\left[(1+O/F)/(1+2O/F)\right]L^*c^*_{exp}} \qquad (14a)$$

$$f = 0.48\frac{(G_o+G_f)RT_{ave}}{c'LP_c} = 0.48\left(2+\frac{1}{O/F}\right)\frac{G_oRT_{ave}}{c'LP_c} \qquad (14b)$$

The oscillation frequency as a function of the boundary delay time predicted by the TC coupled theory along with data form the hybrid motor development programs are plotted in Figure 12. Note that we have used a boundary layer delay constant value, c', of 2.01 for all motor tests in order to obtain the best fit between the theory and test results. Please note that this experimental value for c' is the same order of magnitude with the rough estimate (i.e. ~0.55) for a boundary layer with no blowing and no combustion.

Considering the wide range of test conditions, the agreement between the measured pressure oscillation frequencies and the TC coupled model predictions is surprisingly good. Note that the comparison includes 43 motor tests

- Using results from 4 different development and research programs
- Using 3 separate oxidizers (i.e. LOX, GOX and N_2O)
- Covering a wide range of motor dimensions (i.e. from 5" OD Arizona state motor up to 72" OD AMROC motor)
- Using many different fuel compositions (i.e. HTPB, HTPB/ESCOREZ, HTPB/DDI/ESCOREZ, 2 paraffin-based formulations)

- Covering a wide range of operating conditions.

Equation 14a indicates that for motors operating at the similar O/F, the oscillations frequency is inversely proportional to the L^* of the motor. This conclusion is consistent with the previous results reported in the literature. Similarly Equation 14b shows for motor operating at equal oxidizer mass fluxes, chamber pressures and O/F the oscillation frequency decreases with increasing fuel grain length. In order to prove that motor length plays a critical role setting the oscillation frequency, we have plotted the Ames motor data, which contains two sets of grain lengths, by removing the length effect from the scaling law. This resulted in an increase in the scatter in the frequency data indicating the importance of the grain length. A similar check to confirm the importance of length can be conducted by comparing the JIRAD and HPDP motor tests (i.e. ran with grains 102 inches long) with the Ames paraffin tests (i.e. ran with grains 32 or 45 inches long) that were conducted under very similar operating conditions. For example comparing test 8 of the HPDP program to paraffin based motor test 4P-01 shows that grain length must be included in the scaling law in order to explain the discrepancy in the oscillation frequencies for these tests. The same conclusion can be drawn by comparing test 2 of HPDP program to the test Ames test 4L-08.

TC coupled theory predicts oscillations of the regression rate/fuel mass generation rate and would be observed directly in a hybrid motor as the radial oscillations of the diffusion flame within the boundary layer. The gas dynamic model converts the fuel mass generation rate oscillations to the chamber pressure oscillations. It is expected that a system operating at higher O/F ratios would produce less chamber pressure oscillations since fuel mass constitute a smaller fraction of the total mass expelled from the nozzle. This fact is observed in NASA Ames motor tests, namely high O/F motors, in general, presented lower amplitudes chamber pressure oscillations compared to the mean chamber pressure.

The simple linear model presented in this paper successfully explains the generation of small amplitude low frequency oscillations and the scaling of the frequency. But it also falsely predicts an indefinite growth of chamber pressure oscillations. In reality, the nonlinear mechanisms that exist in a hybrid motor would limit the indefinite growth of the oscillations and result in limit cycle oscillations that are commonly observed in motor tests. Moreover the simple theory does not explain when these low frequency instabilities will take place and what their amplitudes would be. It has been shown in the hybrid development programs that the fore end configuration/volume of the motor plays a paramount importance in setting the amplitude of the low frequency instabilities. The motor tests indicated that, at least for gaseous motors, axial injectors result in more stable operation compared to the radial or conical injection of the oxidizer.

A natural explanation for these observations is that the TC coupled instability mechanism almost always exist in hybrid systems, but the amplitude of the limit cycle oscillations will depend on the excitation level by the disturbances in the right frequency range. We believe that the fore end fluid dynamics (i.e. vortex shedding) is the primary source of disturbances in a hybrid rocket. For example changing the injection scheme of the oxidizer from axial to radial, may introduce a flow disturbance component that is preferred by the TC coupled system. If one assumes that all the low frequency oscillations are developed by the fluid mechanics at the fore end of the motor, one would fail to explain the length effect on the oscillation frequency. Also all oxidizer injection schemes under identical motor operating conditions seem to produce the same oscillation frequency. This fact is also difficult to explain by the assumptions that all the oscillations are produced from the fluid dynamic events at the fore end of the motor, since the injection scheme should alter the fluid mechanics significantly (i.e. vortex shedding frequency).

We would like to note that most of musical instruments also work on the same principle[23]. For example in a flue organ pipe the column of air inside the pipe is set into vibration (i.e. at its natural frequencies) by an edge tone which is produced by a jet of air that impinges on a carefully designed lip. The vortex shedding at the lip sets the edge tone which itself excites the natural modes in the pipe. Note that in the case of an organ pipe the jet speed and the lip geometry is carefully selected for the pipe length such that the edge tone produced at the lip contains a large component at the natural frequency of the pipe that needs to be excited. In this organ pipe analog, the lip is the fore end of the motor (i.e. geometry, injection scheme, velocity etc) and the organ pipe is the hybrid system modeled by the TC coupled theory.

11) Conclusions:

The following conclusions can be drawn from the results of the TCG coupled model:

- A plausible mechanism that generates low-frequency chamber pressure oscillations is suggested. This mechanism is due to the coupling of the thermal lags, the gas phase combustion and gas dynamic sub-systems of the hybrid rocket. The physical transient model of the motor is presented in a mathematical formalism that allows one to estimate the expected oscillation frequency. The amplitude of the oscillations can not be determined by this linear model.
- The oscillation frequency estimated by the model is in very good agreement with the motor test data from several programs utilizing three distinct oxidizers, several fuel formulations, a wide range of motor dimensions and operating conditions. We suggest the following equation as a universal scaling law for the primary hybrid oscillation frequency:

$$f = 0.239 \left(2 + \frac{1}{O/F}\right) \frac{G_o RT_{exc}}{L\, P_c} \qquad (15)$$

$RT_{exc} = 6.39\ 10^5$ (m/sec)^2 for GOX/LOX systems

$RT_{exc} = 5.11\ 10^5$ (m/sec)^2 for low energy oxidizers systems such as N_2O

- This mode of instability is common to all kind of hybrids: liquefying or conventional fuels, liquid oxidizer or gaseous oxidizers. It is reasonable to believe that this low frequency mode is present in every hybrid system to some extent. Some motors are more unstable compared to the others because these motors do possess more disturbances to excite the TC coupled oscillations. For example the oxidizer injector configuration or pre-combustion chamber geometry affects the scale and the frequency of the disturbances that would excite the commonly observed low frequency mode. For this reason the design of the fore end of the motor has been critical in controlling the stability of the system.
- Even though the linear theory very successfully predicts the oscillation frequency of the chamber pressure, it fails to establish an estimation process for the amplitude of the oscillations. The theory predicts an unlimited growth of the oscillations. In reality the amplitude of the chamber pressure fluctuations will be limited by nonlinear effects that are not covered in the linearized TC coupled theory.
- It has been shown that the longitudinal acoustic oscillations that are commonly coexist with the low frequency oscillations can be generated by the excitation induced by the nonlinear waveforms of the low frequency chamber disturbances. In short, it is plausible that high frequency acoustic modes are driven by the low frequency oscillations.

12) Acknowledgement

Part of this work was carried out under cooperative agreements NAG3-2615 with the NASA Glenn Research Center and agreement NCC2-1172 and NCC 2-1300 with the NASA Ames Research Center. This work was also supported by NASA grant NAG3-2884.

13) References

1. M. W. Beckstead and E. W. Price, "Nonacoustic Combustion Instability", AIAA Journal Vol. 5, No. 11 p. 1989, 1967.

2. R. S. Brown and R. J. Muzzy, "Linear and Nonlinear Pressure Coupled Instability of Solid Propellants", AIAA Journal, p 1492, 1970.

3. F. E. C. Culick and V. Yang, "Combustion Instabilities in Liquid Rockets", Progress in Astronautics and Aeronautics, Vol.169, pp 3-37, 1995.

4. D. M. Gutlric and R. S. Wolf, "Non-Acoustic Combustion Instability in Hybrid Rocket Motors", N 91-24250, 1991.

5. T. A. Boardman, R. L. Carpenter and S. E. Claflin, "A Comperative study of the Effects of Liquid-Versus Gaseous-Oxygen Injection on Combustion Stability in 11-inch-Diameter Hybrid Motors", AIAA paper No97-2936, AIAA/SAE/ASME/ASEE 31 st Joint Propulsion Conference and Exhibit, July 1997.

6. Shane De Zilwa, M. Arif Karabeyoglu and Greg Zilliac, "Combustion Oscillations in High Regression Rate Hybrid Rockets", AIAA paper 2003-4465, Joint Propulsion Conference, Huntsville/Alabama, 2003.

7. B. Greiner and R. A. Frederick,Jr, "Experimental investigation of Labscale Hybrid Instability", AIAA paper, No. 94-2878, 1994.

8. T. A. Boardman, D. H. Brinton, R. L. Carpenter, T. F. Zolods, "An Experimental Investigation of Pressure Oscillations and Their Suppression in Subscale Hybrid Rocket Motors", AIAA paper 95-2689, 1995.

9. R. M. Jenkins, J. R. Cook, "A Preliminary Analysis of Low Frequency Pressure Oscillations in Hybrid Rocket Motors", AIAA paper No. 95-2690, 1995.

10. B. Greiner and R. A. Frederick,Jr, "Hybrid Rocket Instability", AIAA paper, No. 93-2553, 1993.

11. C. Wooldridge, G. A. Marxman and R. Kier, "Investigation of Combustion Instability in Hybrid Rockets", NASA CR-66812 Final Report, 1969.

12. C. Wooldridge and G. A. Marxman, "Combustion Instability and the Role of Chemical Kinetics in Hybrid Combustion." AIAA Journal No. 68-498, 1968.

13. Karabeyoglu M. A., "Transient Combustion in Hybrid Rockets", Stanford University Ph.D. thesis, August 1998.

14. Karabeyoglu, M. A. and Altman, D., "Dynamic Modeling of Hybrid Rocket Combustion", *AIAA Journal of Propulsion and Power* Vol. 15, No 4, 1999, p. 562-571.

15. Marxman G. A., C. E. Wooldridge and R. J. Muzzy, "Fundamentals of Hybrid Boundary Layer Combustion", Progress in Astronautics and Aeronautics, Vol.15, 1964, p. 485-522.

16. Parikh, P. G., Jayaraman, R., Reynolds, W. C. and Carr L. W., "Transient Response of a Turbulent Boundary Layer" FED-Vol 12, ASME, New York, 1984, p. 31.

17. Schlichting, H., "Boundary Layer Theory", McGraw Hill, Chapter 21, 1955.

18. Moelwyn-Hughes, E.A., "Physical Chemistry", Chapter 6, Second Revised Edition, Pergamon Press, 1961

19. Altman, D. and Humble, R. "Hybrid Rocket Propulsion Systems" in Space Propulsion Analysis and Design, McGraw Hill, 1995, p382.

20. M. A. Karabeyoglu, Greg Zilliac, Brian J. Cantwell, Shane DeZilwa and Paul Castellucci "Scale-up Tests of High Regression Rate Liquefying Hybrid Rocket Fuels", AIAA-2003-1162, 41st Aerospace Sciences Meeting and Exhibit, Reno Nevada, January 2003.

21. T. A. Boardman, R. L. Carpenter, B. E. Goldberg, and C. W. Shaeffer, "Development and Testing of 11- and 24- Inch Hybrid Motors Under the Joint Government/Industry IR&D Program", AIAA Paper Number 93-2552, AIAA/SAE/ASME/ASEE 29 th Joint Propulsion Conference and Exhibit, June 1993.

22. J. M. Pucci, "The Effects of Swirl Injector Design on Hybrid Flame-Holding Combustion Instability", AIAA Paper No. 2002-3578, AIAA/SAE/ASME/ASEE 38th Joint Propulsion Conference and Exhibit, July 2002.

23. Jeans, James, "Science and Music", Dover Publications Inc., New York, 1968.

24. L. Crocco and S. I. Cheng, " Theory of Combustion Instability in Liquid Propellant Rocket Motors", Agardograph No. 8, 1956.

25. H. Lomax and T. Pulliam, "Finite Difference Methods for Fluid Dynamics", 1993.

14) Appendix

In our gas dynamic model the motor is divided into four subsections: 1) pre-combustion chamber, 2) port volume, 3) post-combustion chamber, 4) nozzle. Each component is approximated appropriately with one or zero spatial dimensional models. The subscripts 1 and 2 are used for the physical properties in the pre and post combustion chambers respectively. Various stations of significance are also distinguished by use of subscript notation. Namely the entrance station of the gaseous oxidizer into the system is represented by a subscript o, the nozzle entrance is denoted by n and the port entrance and exit are shown by a and b, respectively. Our models for these subsections are discussed in the next section.

Pre-Combustion Chamber

We use a zero dimensional gas dynamic model for the pre-combustion chamber. Thus the momentum equation and the energy equations reduce to the mean state information of the pressure and temperature in this volume. But, the mass balance equation is nontrivial and it can be written as

$$V_1 \frac{d\rho_1}{dt} = \dot{m}_o - \dot{m}_a . \qquad \text{(A.1)}$$

Note that the size of the volume is assumed to be constant over the burn time. We further assume a constant molar mass and a polytropic process, $P \propto \rho^{n_p}$ in the chamber. Here n_p is the polytropic exponent. We believe that these are reasonable assumptions for this relatively cold volume which accommodates negligible combustion. Under these stated conditions and with the use of the ideal gas law, equation A.1 can be reduced to

$$a_1 \frac{dP_1}{dt} = \dot{m}_o - \dot{m}_a \text{ where } \quad a_1 = \frac{V_1}{n_p R_1 T_1} . \quad \text{(A.2)}$$

Port Chamber

In our model we treat the port as a quasi-1D tube with continuous mass and heat addition. The conservation of mass can be written as the following differential equation.

$$\frac{\partial \rho}{\partial t} = -\frac{\partial G}{\partial z} + \dot{m}_f \qquad \text{(A.3)}$$

Here $\dot{m}_f$ is the mass generated at the axial location z of the port. At this stage we prefer to express the mass generation term in the general functional form.

$$\dot{m}_f = f(G, z)$$

The momentum equation in the port can be written in terms of the local mass flux, G, the local pressure, P and the local density, ρ.

$$\frac{\partial G}{\partial t} = -\frac{\partial (G^2/\rho)}{\partial z} - \frac{\partial P}{\partial z} - \left(\frac{C_f C}{2A_p}\right)\frac{G^2}{\rho} \qquad \text{(A.4)}$$

Note that the last term in this expression is included to capture the effect of the skin friction on the force balance. Here C_f stands for the skin friction coefficient at location z, A_p as the port area and the C for the circumference of the port. All the geometrical properties are assumed to be independent of time and axial dimension. This is a reasonable approximation for typical hybrids which posses a uniform port diameter distribution along the length and also a slow variation of the port geometry[15].

We further assume that the ideal gas law holds locally in the port.

$$P = \rho RT \qquad \text{(A.5)}$$

The closure of the system requires the energy equation. For the sake of simplicity we replace the energy equation with the following linear variation of temperature gas constant product in the port.

$$RT(z) = (RT)_1 + ((RT)_2 - (RT)_1)z/L \qquad \text{(A.6)}$$

Note that for the simplicity of notation we treat the gas constant temperature product as a single dependent variable.

Furthermore we assume that the gas constant temperature product at the exit of the port volume is a fraction of the nozzle entrance value RT_c which can be calculated from the equilibrium chemistry at the operating O/F ratio of the motor.

$$RT_2 = f_b RT_c \qquad \text{(A.7)}$$

In short, we specify the whole temperature field in the motor chamber for a given operating point and we ignore the variations in the temperature field during the transients. In that respect 2V-port is an isothermal gas dynamic model.

Post-Combustion Chamber

Similar to the pre-combustion chamber treatment, we assign uniform thermodynamic properties for the gas in the post-combustion chamber volume. Therefore the dynamics can be represented with the mass balance which takes the following form after the fixed volume assumption.

$$V_2 \frac{d\rho_2}{dt} = \dot{m}_b - \dot{m}_n \qquad \text{(A.8)}$$

Here $\dot{m}_b$ is the mass flow rate entering the hot volume and $\dot{m}_n$ is the mass flow rate exiting the volume through the nozzle. Note that we have inherently assumed that post-combustion chamber behaves like a well stirred reactor with the reactions fast compared to the transient rates of concern. Equation A.8 can be written as

$$a_2 \frac{dP_2}{dt} = \dot{m}_b - \dot{m}_n \quad \text{where} \quad a_2 = \frac{V_2}{RT_2}. \qquad \text{(A.9)}$$

We have approximated the gas constant temperature product in the post-combustion chamber with product at the port exit.

Nozzle

We first assume that the nozzle flow is quasi-steady which is only valid at very slow transients. We also assume that through out the operation of the motor, the nozzle is always choked, namely at any time the ratio of the chamber pressure to the ambient pressure is larger

than the critical value associated with the properties of the expanding gas. After these simplifying assumptions the nozzle flow rate can be expressed with use of the classical quasi-1D gas dynamic formula

$$\dot{m}_n = \frac{A_n \Gamma_c P_2}{\sqrt{RT_c}} \tag{A.10}$$

where

$$\Gamma_c = \sqrt{\gamma_c}\left(\frac{2}{\gamma_c+1}\right)^{\frac{\gamma_c+1}{2(\gamma_c-1)}}$$

Here γ_c is the ratio of the specific heats of the combustion products.

At moderate frequency oscillations (such as the acoustic modes of the motor), the acoustic admittance of the nozzle must be considered and a more sophisticated behavior must be modeled. For our purposes, it is adequate to adapt Crocco's expression[24] for the nozzle transfer function which is valid for small deviations from the mean chamber pressure and for moderate frequencies.

$$\frac{\tilde{\dot{m}}_n}{\tilde{P}_2} = \frac{A_n \Gamma_c \tilde{P}_2}{\sqrt{RT_c}} + k_n \frac{d}{dt} \tag{A.11}$$

Here k_n represents the effect of inertia of the gas in the convergent portion of the nozzle in causing a phase difference between the oscillation of the velocity and pressure at the entrance of the nozzle.

$$k_n = \frac{c_*}{\gamma_c\left(c_*^2 - u_e^2\right)} \int \left(\frac{c_*}{u} - \frac{\gamma_c - 1}{2}\frac{u}{c_*}\right) dx \tag{A.12}$$

This integration is performed on the whole convergent portion of the nozzle. Note that c_* is the critical sound velocity, u is the local gas velocity in the nozzle, u_e is the gas velocity at the nozzle entrance.

Equations A.9 and A.11 and the ideal gas law can be combined to relate the pressure perturbation directly to the mass flow rate perturbation at the exit of the port.

$$\left(a_2 + k_n\right)\frac{d\tilde{P}_2}{dt} = -\left[\left(\frac{V_2}{(RT_c)^2}\right)\frac{d(RT_c)}{dt} + \frac{A_n \Gamma_c}{\sqrt{RT_c}}\right]\tilde{P}_2 + \dot{m}_b \tag{A.13}$$

Note that a fraction of the nozzle volume is added to the post-combustion chamber volume to account for the inertial effects of the gas in the nozzle. For typical hybrids the effective nozzle volume is small compared to the post-combustion chamber volume. We finally indicate that for our isothermal treatment the temperature derivative term is identically zero.

Equation A.13 includes some properties of the combustion products which are not known offhand. These properties are calculated from chemical equilibrium considerations with use of the code STANJAN for the selected propellants. A sample calculation result of the product, RTc with the motor O/F ratio for HTPB-oxygen system is given in Ref. 13.

Solution Techniques

In this section we develop small perturbation solutions and also numerical solutions for the system of equations derived for the 2V-port model .

Perturbation Solutions

We determine perturbation solutions around a nominal operating point of the rocket for the gas dynamic system of equations described in the previous paragraphs. These perturbation solutions will be used to obtain a transfer function representing the linear response of the gas dynamic system. The transfer function uses the oxidizer mass flow rate as the input and the system pressure for the output. The details of the derivation are shown in Ref. 13.

The transfer function specifically between the oxidizer mass flux input and the pre-combustion chamber pressure output can be written as

$$\Theta_1 = \frac{RT_1\{\Delta + [(F_{TC} - a_\Phi) + 2b_\Phi(L_2 s + e)]\tanh(\Delta L/2)\}\ I}{[(L_1 + L_2)\ s + e]\ \Delta + [L_1(F_{TC} - a_\Phi) + 2]\ s + [2L_1 b_\Phi s - (F_{TC} - a_\Phi)]\ (L_2 s + e)\tanh(\Delta L/2)} \quad \text{(A.14)}$$

This function also represents the overall nature of the response for gas dynamic system. Similar expressions for the other variables can be also derived, but for the purpose of our arguments this expression is adequate.

Numerical Simulations

In order to check the validity of the assumptions used in the perturbation solutions, we also perform numerical simulations on the 2V-port model described in the previous section. We start with the finite differencing of the special derivative terms and use the second order central differencing over a uniform mesh along the axis of the port[25]. For the time marching we use the Runge-Kutta fourth order method. The boundary conditions for the port equations are obtained from the pre and post combustion chamber dynamic equations. The numerical method used in the calculations gave stable and accurate results for a typical time step of 3×10^{-4} seconds and 80 mesh points in the port. The details of the numerical scheme is discussed in Ref 13.

The simulation code is applied to various transient events such as the throttling and the sinusoidal oxidizer flow rate case. Some of the results are discussed in the following section.

Discussion of Results for Pure Gas Dynamics

The response of the gas dynamic system for a hybrid motor can be deduced from the gas dynamic system transfer function. For example, the stability features of the system are revealed by the roots of the denominator of the transfer function which is the characteristic equation. However any investigation of the gas dynamic system response requires an input for the combustion response that is represented by the F_{TC} term.

In this section we use the simplest quasi-steady combustion model. Namely, all the transient effects including the thermal lags in the solid and also the boundary layer delays except the gas dynamics are ignored in this model. For that reason, this model which does not allow any dynamic coupling between the sub-systems of the rocket is highly desirable to isolate the investigations to purely gas dynamic phenomena. The combustion response function can easily be derived from the general regression rate law after linearization and Laplace transformation.

$$F_{TC} = a_1 n \bar{G}^{n-1} \quad \text{(A.15)}$$

For the case of the quasi-steady combustion the gas dynamic system transfer function is plotted in Figure 13. The operational parameters of this motor are discussed in Ref. 13. The plot shows a pole on the negative real axis and a row of imaginary poles also in the negative real half plane. The real pole resembles the volumetric capacity of the chamber, whereas the imaginary poles represent the longitudinal acoustic nature of the cavity. Note that all the poles have negative real parts, namely the both acoustic and also the global response components decay in time. The conclusion is that the pure gas dynamic system is stable in nature.

In order to test the validity of the transfer function we consider the trivial case of no mass addition and no temperature or velocity gradients in the port. In this case the transfer function simplifies to

$$\Theta_1 = \lim_{(F_{TC} - a_\Phi)\to 0} \frac{RT_c I}{[(L_1 + L_2)\ s + e] + \dfrac{2s}{(F_{TC} - a_\Phi)}\tanh[(F_{TC} - a_\Phi)L/2]}. \quad \text{(A.16)}$$

After the application of the L'Hospital's rule one obtains the well known transfer function for a simple single volume system.

$$\Theta_1 = \frac{RT_c I}{(L_1 + L_2 + L)\, s + e} = \frac{(RT_c / \theta\, c^*)}{\tau_f s + 1} \qquad \text{(A.17)}$$

Here $\tau_f = L^*/c^*$ is the characteristic filling time of the motor chamber. The other parameters are defined as $L^* = V/A_p$ and $c^* = \Gamma_c\sqrt{RT_c}$ which are commonly used in rocket literature. Note that the total volume of the motor combustion chamber can be written as $V = (L_1 + L_2 + L)A_p$. This is the transfer function generally used (especially in the industry) in hybrid dynamic modeling.

The preceding equation does not predict the filling/emptying time scale of a hybrid rocket accurately. For that reason we develop a better estimate by the following argument. In the region of the s plane that the pole for the filling/emptying process is expected to be located, the following approximations can be made.

$$a_\phi \cong \frac{\beta}{RT_{inc}},\quad b_\phi \cong 0,\quad \Delta \cong \left|a_\phi - F_{TC}\right| \qquad \text{(A.18)}$$

Under these approximations the gas dynamic transfer function simplifies to

$$\Theta_1 = \frac{RT_1\left\{1 + \tanh\left[\left(F_{TC} - a_\phi\right)L/2\right]\right\} I}{\left\{L_1 + L_2 + \left[L_1 - L_2 + 2/\left(F_{TC} - a_\phi\right)\right]\tanh\left[\left(F_{TC} - a_\phi\right)L/2\right]\right\} s + e\left\{1 - \tanh\left[\left(F_{TC} - a_\phi\right)L/2\right]\right\}}. \qquad \text{(A.19)}$$

Note that since $F_{TC} - a_\phi$ term is independent of s, this transfer function represent the behavior of a first order system with a characteristic time of

$$\tau_f = \frac{L_1 + L_2 + \left[L_1 - L_2 + 2/\left(F_{TC} - a_\phi\right)\right]\tanh\left[\left(F_{TC} - a_\phi\right)L/2\right)}{e\left\{1 - \tanh\left[\left(F_{TC} - a_\phi\right)L/2\right]\right\}}. \qquad \text{(A.20)}$$

The throttling response for a throttling ratio of 1.2 of the motor with the same specifications is calculated with different methods and plotted in Figure 14. Figure shows the time variation of the non-dimensional pre-combustion chamber pressure defined as $\left(P_1(t) - P_1^i\right)/\left(P_1^f - P_1^i\right)$ where P_1^i is the initial pressure and P_1^f is the final pressure. The striking observation is that the perturbation solution with the filling time defined by equation A.20 is in excellent agreement with the numerical simulation result. This shows that equation A.20 gives a good estimate for the filling time of the motor chamber within the context of the 2V-port model. The response according to the simple transfer function is also shown in Figure 14. It is obvious from the figure that the simple filling time argument for the hybrid combustion chamber is not valid.

Another observation from Figure 14 is that the numerical simulation result shows oscillatory behavior in the early stages of the throttling event. This oscillatory behavior is due to the excitation of the acoustic modes of the cavity by the disturbance caused by the sudden increase in the oxidizer mass flow rate. The oscillation frequency and the damping time scale of this mode of motion is consistent with the longitudinal acoustic mode findings for the same motor.

This kind of behavior is commonly observed in AMROC DM-01 motors[4]. Namely, a nonlinear disturbance causes the well damped oscillation of the chamber pressure at the longitudinal acoustic frequencies. The exciting disturbances in the actual tests are believed to be caused by: 1) a sudden blockage of the nozzle throat area by some disintegrated fuel fractions, 2) the ignition of a bulk of fuel oxidizer mixture

captured in the pre-combustion chamber or 3) the low frequency oscillations of chamber pressure.

We compare the predictions of our gas dynamic model for the acoustic frequencies of the chamber with the AMROC DM-01 motor test data. Table 7 shows the first five longitudinal frequencies determined by the perturbation solutions. Since our model is isothermal, these frequencies are corrected by multiplying with the factor of $\sqrt{\gamma}$. An average γ value of 1.2 is used for the calculations. Note that the corrected frequencies falls in the range of observed frequencies for every calculated acoustic mode.

The gas dynamic code developed to perform simulations on the 2V-Port model is used to confirm the findings of the perturbation solutions on the frequency response of the system. In the simulations, sinusoidal oxidizer mass flow rate inputs at various frequencies are applied as the forcing function and the phase and the amplitude of the chamber pressure oscillations are determined. The agreement between the perturbation solutions and the numerical simulations for the frequency response of the system is also found to be satisfactory.

The simulation code is also used to investigate the response of the gas dynamic system to a disturbance. The oxidizer mass flow input is suddenly increased 10% above its operating value and held at its elevated level for 0.03 seconds before its suddenly reduced to its original value. The pressure time history for this simulation is shown Figure 15. It is clear that the disturbance excites the acoustic modes of the chamber similar to the previous observations. These exited modes decay in a moderate time scale as it was observed in the AMROC tests. A similar simulation is performed to determine the effect of nozzle blockage on the stability by reducing the nozzle throat area for a brief period of time. The results for the nozzle area perturbation case are identical in nature to the results of the oxidizer mass flow rate perturbation. In short, a nonlinear disturbance causes the ringing of the hybrid chamber which decays in time.

Finally a simple delay (τ_{M1}) on the combustion response is applied to the gas dynamic system.

$$F_{TC} = a_1 n \bar{G}^{n-1} e^{-\tau_{M1} s} \qquad \text{(A.21)}$$

Both the perturbation solutions and also the numerical simulations indicate that any positive combustion delay have negligible effect on the stability nature of the system.

15) Tables and Figures:

Physical Phenomenon:	Time Scale:	Explanation:
1) Solid phase kinetic times	$\tau_{sp} < 10^{-3}$ sec	Degradation mechanisms of the polymer
2) Gas phase kinetic times	$\tau_{gp} < 10^{-3}$ sec	Hydrocarbon combustion mechanisms
3) Feed system response times	(Varies greatly from system to system)	Response time of the feed system
4) Evaporation times	$\tau_{evap} = f(U_o, T_1, \Delta P)$	Evaporation process of the liquid oxidizer
5) Thermal lags in solid	$\tau_{sl} \propto \kappa / \dot{r}^2 \approx 10^{-1}$ sec	Thermal profile changes in the solid grain
6) Boundary layer diffusion times	$\tau_{bl} \propto L / u_e \approx 10^{-1}$ sec (Varies greatly form case to case)	Turbulent boundary layer diffusion processes
3) Acoustic times (longitudinal)	$\tau_a \propto L / c \approx 10^{-3}$ sec (Varies greatly form case to case)	Propagation of the acoustic waves
7) Gas dynamic filling times	$\tau_{fill} \propto L^* / \dot{c}^* \approx 10^{-1}$ sec (Varies greatly form case to case)	Global mass flow balance

Table 1: The transient time scales of various phenomena in a typical hybrid rocket. Only the last four are modeled in this paper.

AMROC Motor (thrust)	O/F	c^*_{theo} (ft/sec)	c^*_{exp} (ft/sec)	L^* (in)	f (Hz)	τ_{M2} (msec)
S Motor (10k)	1.45	5584	5361	570	11	48.9
Half-Scale (33k)	1.45	5584	5361	1305-1430	4.8	117.4
H-500 (75k)	1.45	5584	5361	1770-2340	4.0	176.3
DM-01 (250k)	1.55	5700	5472	2168	2-3.5	204.8

Table 2: Summary of parameters used in the frequency estimations for AMROC motors.

Test No.	$\overline{D}$ (in)	$\dot{m}_o$ (lb/sec)	G_o (lb/ in^2-sec)	G_t (lb/ in^2-sec)	P_c (psi)	O/F	f (Hz)	ΔP_{osc} (psi)	τ_{M2} (msec)
1 (GOX)	4.25	6.0	0.423	0.571	600	2.85	13	200	48.8
2 (GOX)	4.25	5.7	0.402	0.541	550	2.89	8	300	47.2
7 (GOX)	4.20	4.7	0.339	0.458	440	2.89	15	100	44.7
8 (GOX)	4.22	5.1	0.365	0.492	260/280	2.87	20	400	25.5
1 (LOX)	-	-	0.222	0.31	435	2.51	8	250	66.2

Table 3: Summary of parameters used in the frequency estimations for the 11 inch Hybrid motor tests. Grain length is 102 inches.

Test No.	$\overline{D}$ (in)	L (in)	$\dot{m}_o$ (lb/sec)	G_o (lb/in^2-sec)	G_t (lb/ in^2 in-sec)	P_c (psi)	O/F	f (Hz)	ΔP_{osc} (%)	τ_{M2} (msec)
3	3.4	102	3.44	0.38	0.527	745	2.6	6-10	15	66.5
4	4.3	102	3.36	0.23	0.325	325	2.4	10-20	20	47.4
6	3.7	102	8.36	0.78	1.024	750	3.2	10-15	12	33.7
7	5.3	102	3.41	0.15	0.22	335	2.1	6-15	15	73.3
8	5.7	102	3.87	0.15	0.209	850	2.6	2-5	60	191.7
9	6.1	102	6.34	0.28	0.392	215	2.6	6-20	33	25.9
15	5.4	108	10.20	0.45	0.599	1025	3.0	4	10	83.9
10	6.1	102	5.93	0.20	0.278	215	2.6	10-25	5	36.5

Table 4: Summary of parameters used in the frequency estimations for the NASA/MSFC 11 inch Hybrid motor tests.

Test No.	$\overline{D}$ (in)	L (in)	$\dot{m}_o$ (lb/sec)	G_o (lb/in^2-sec)	P_c (psi)	O/F	f (Hz)	$\tau_{1/2}$ (msec)
1	2.0	27	3.44	0.29	500	4.0	19	20.6

Table 5: Summary of parameters used in the frequency estimations for the Arizona State Hybrid motor test.

Test No.	L (in)	G_o (lb/in^2-sec)	P_c (psi)	O/F	f (Hz)	$\tau_{1/2}$ (msec)
4F-4	32	0.44	528.0	3.97	41.6	13.5
4F-5	32	0.49	551.0	3.59	39.9	12.6
4F-1b	32	0.20	561.0	2.72	14.4	29.7
4F1-c	32	0.16	542.0	3.06	13.6	36.1
4P-01	45	0.39	318.0	2.69	40.8	12.3
4P-02	45	0.38	993.8	2.48	13.2	38.5
4P-03	45	0.40	939.1	2.65	14.4	35.6
4L-03	45	0.31	641.6	2.69	12.7	30.9
4L-04	45	0.52	656.7	2.66	23.6	18.9
4L-05	45	0.46	649.3	2.72	19.1	21.2
4L-08	45	0.44	525.0	2.64	23.3	17.9
4I-01	45	0.38	318.7	2.40	39.6	12.4
4P-04	45	0.21	159.1	1.73	42.4	10.7
4L-09	45	0.26	265.3	1.54	20.3	13.7
4L-10	45	0.43	590.0	2.89	27.0	18.2
4L-11	45	0.11	213.0	1.56	17.8	27.2
4L-12	45	0.13	301.0	2.01	15.54	32.2
4NF-01	45	0.39	602.2	2.77	22.60	23.1
4NF-02	45	0.22	600.4	2.34	11.10	40.4
4NF-03	45	0.36	500.8	2.96	23.20	21.4
4NF-04	45	0.48	568.5	3.01	32.75	18.0
4L-14	45	0.43	524.5	2.51	25.15	18.0
4ST-02	45	0.45	540.0	2.71	24.86	18.2
4L-15	45	0.31	555.5	2.09	14.94	26.2
4Rep-02	45	0.45	402.3	2.63	36.49	13.5

Table 6: Summary of parameters used in the frequency estimations for the NASA Ames Hybrid motor tests.

Longitudinal Acoustic Mode	Estimated (Isothermal) Frequency (Hz)	Corrected Frequency (Hz)	Observed Frequency (Hz)	Estimated Amplification (1/sec)
1st	48.4	53.0	50-55	-22
2nd	96.7	103.9	100-110	-22
3rd	142.6	156.1	150-165	-21
4th	191.1	209.3	200-220	-19
5th	240.7	263.6	250-275	-18

Table 7: The estimated and observed longitudinal acoustic frequencies for AMROC DM-01 motor.

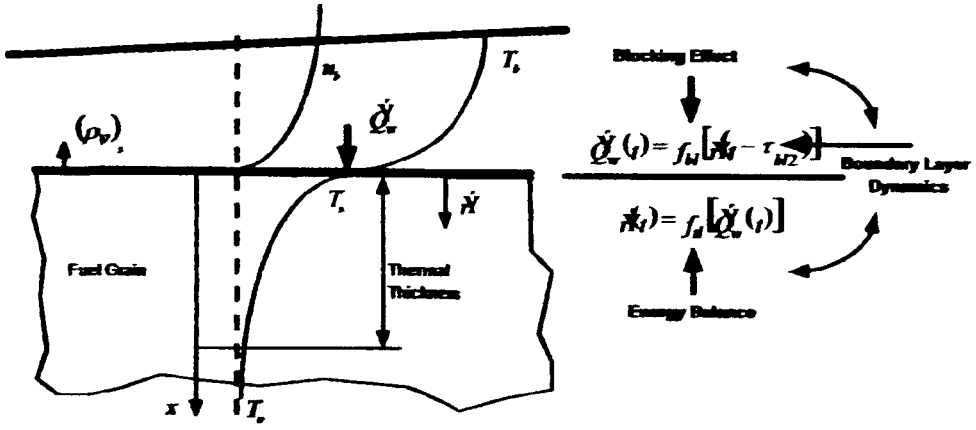

Figure 1: Thermal lag model and TC coupling mechanism.

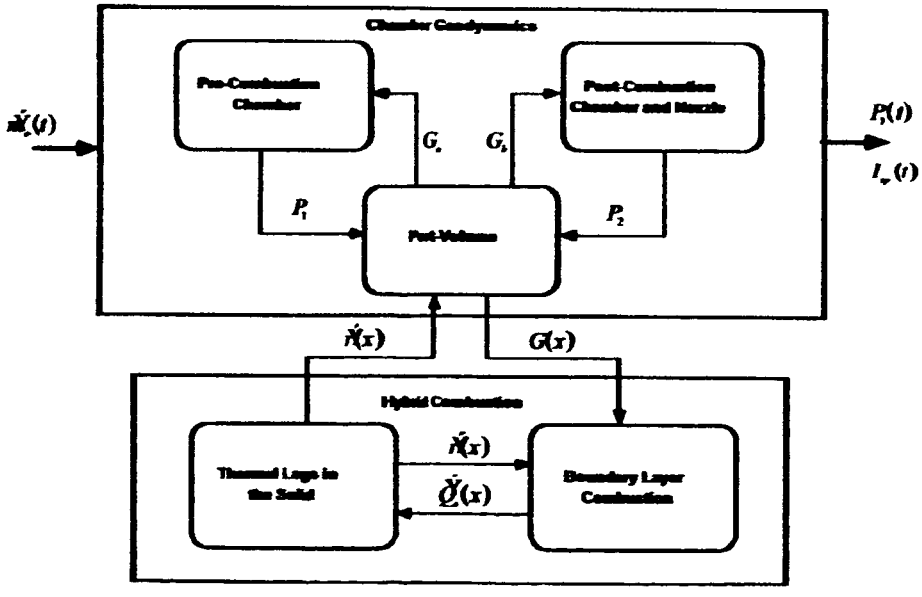

Figure 2. The schematic of the TCG coupled system.

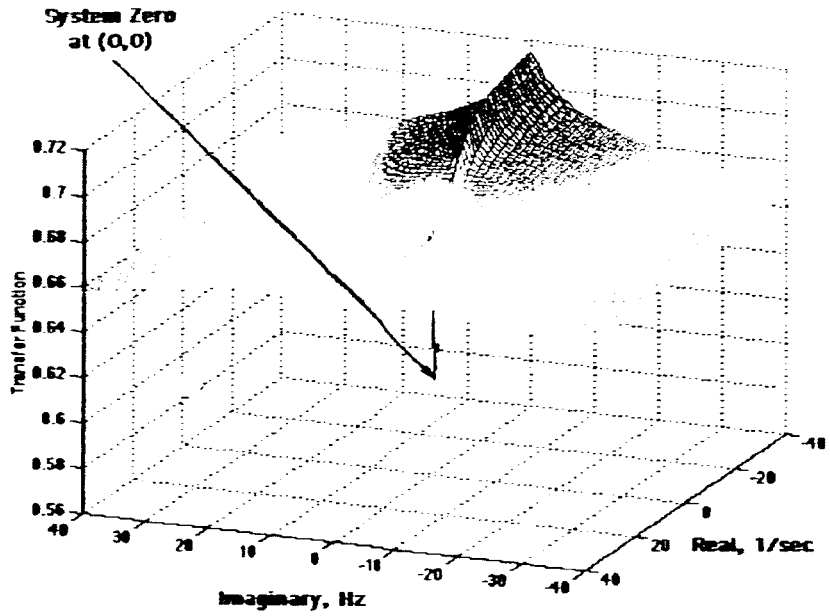

Figure 3: Plot of the transfer function of the TC coupled system with no delays ($\tau_{bf1} = \tau_{bf2} = 0$). This plot is for a HTPB system with E_a=15 kcal/mole.

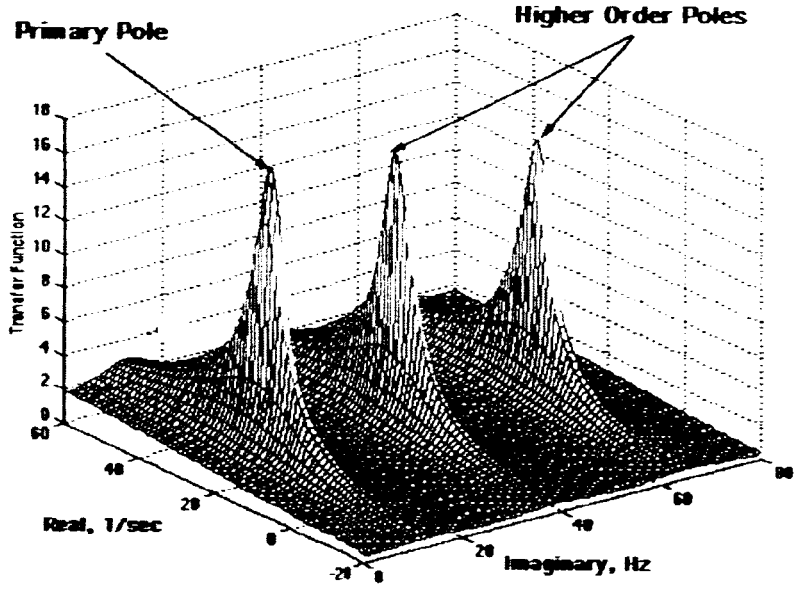

Figure 4: The unstable poles of the TC coupled system in the s plane for $\tau_{bf1} = 0$, $\tau_{bf2} = 38$ msec. This plot is for a HTPB system with E_a =15 kcal/mole.

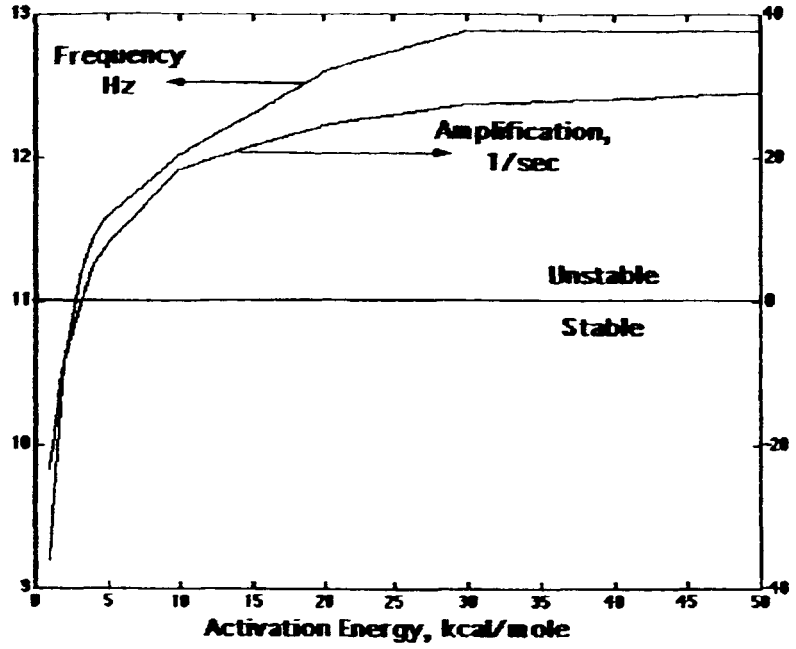

Figure 5: Effect of activation energy on the oscillation frequency and amplification.

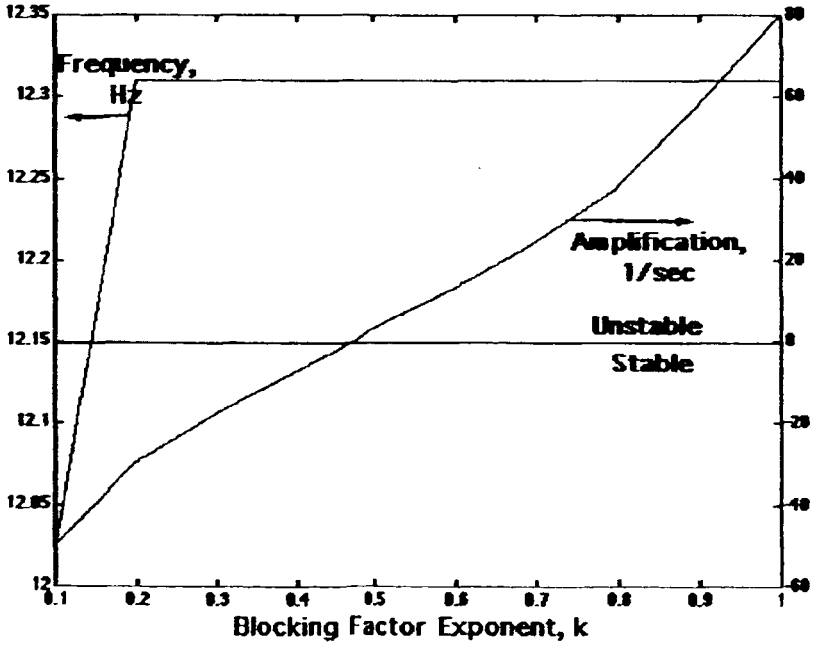

Figure 6: Effect of blocking factor exponent on the oscillation frequency and amplification.

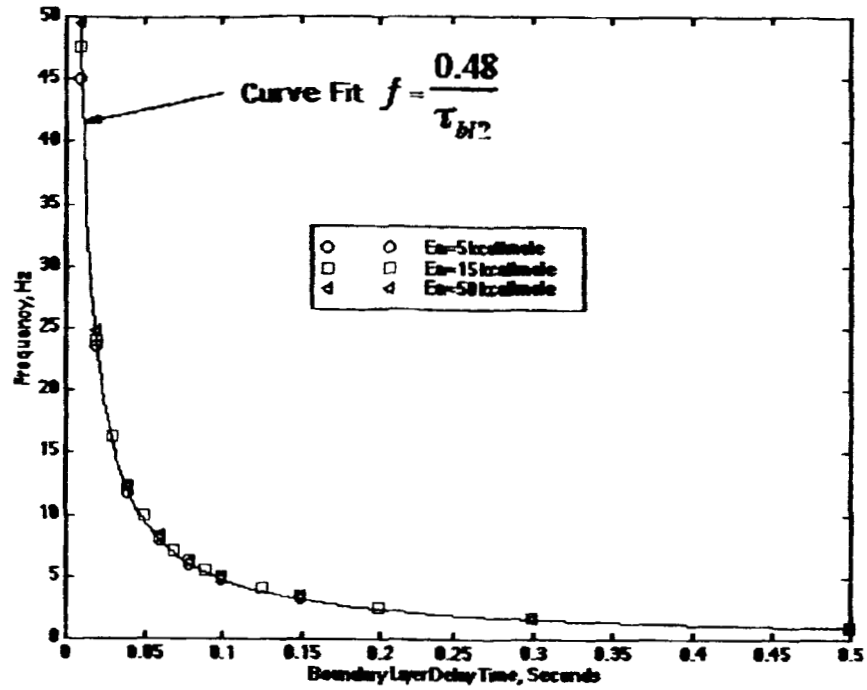

Figure 7: Effect of boundary layer delay time on the oscillation frequency for various activation energies.

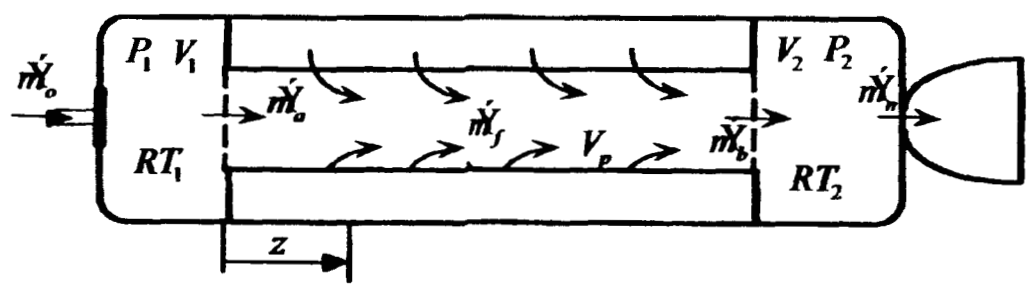

Figure 8: The schematic of the 2V-port model.

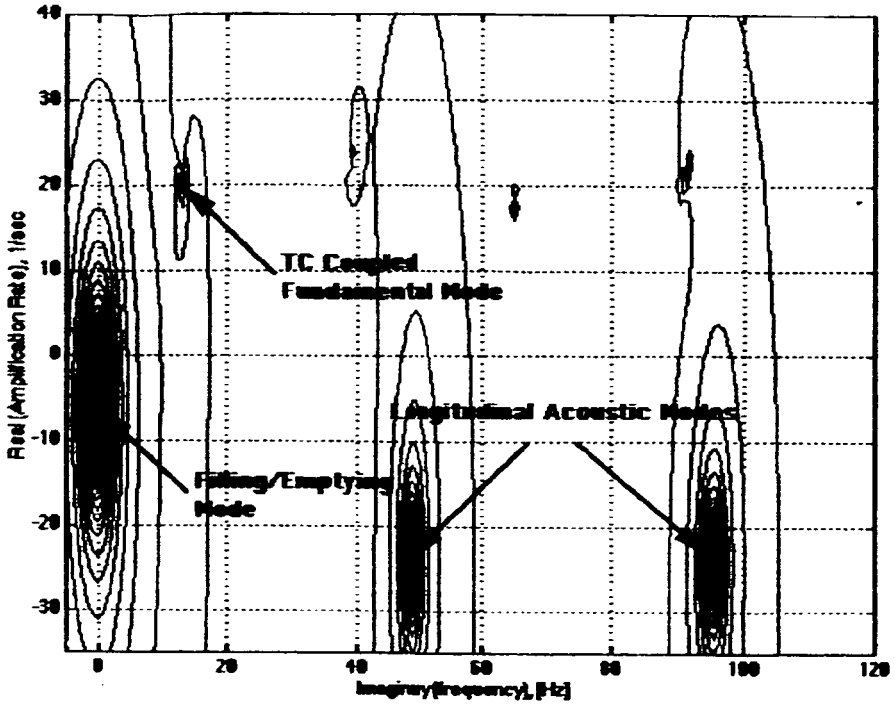

Figure 9: The contour plot of the TCG coupled system with $\tau_{lv2} = 38$ msec. Most of the transient features of a hybrid system can be deduced from the locations of the poles.

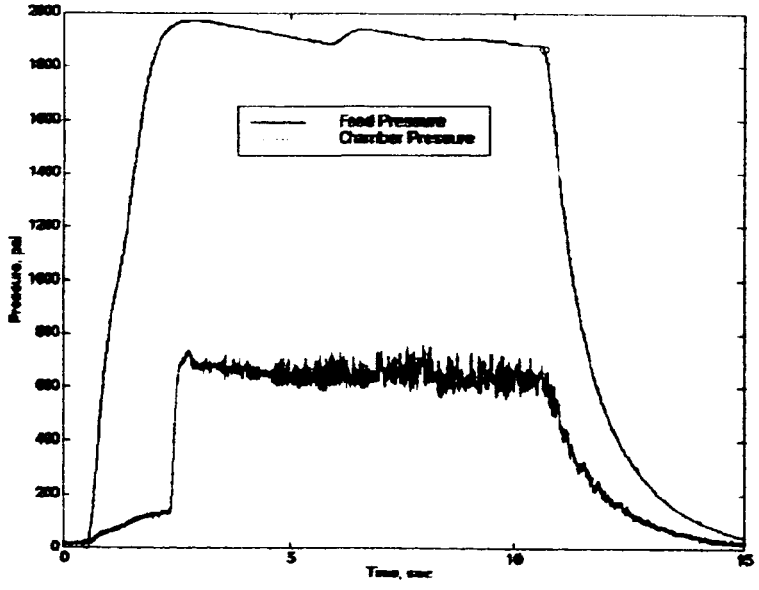

Figure 10: Chamber and feed pressure time traces for the paraffin-based motor test, 4L-05.

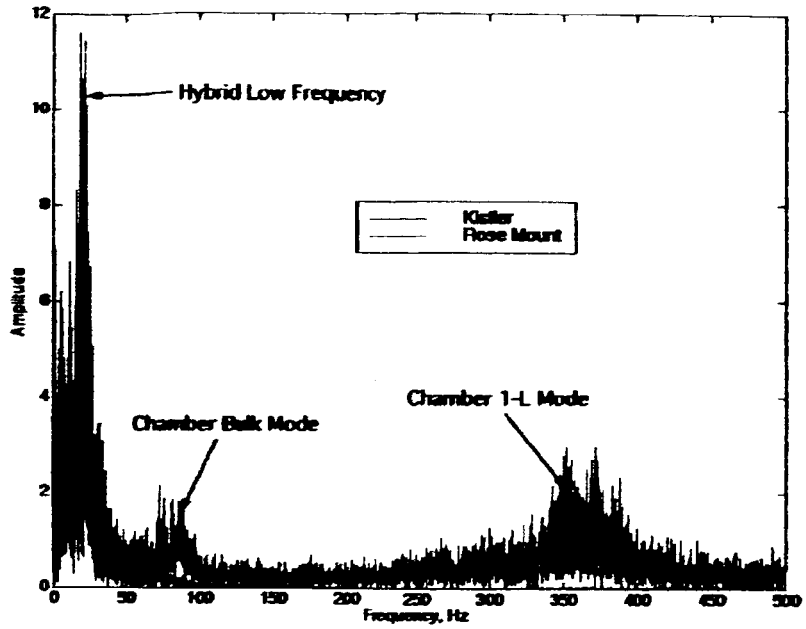

Figure 11: Fourier transform of the chamber pressure for the paraffin-based motor test, 4L-05.

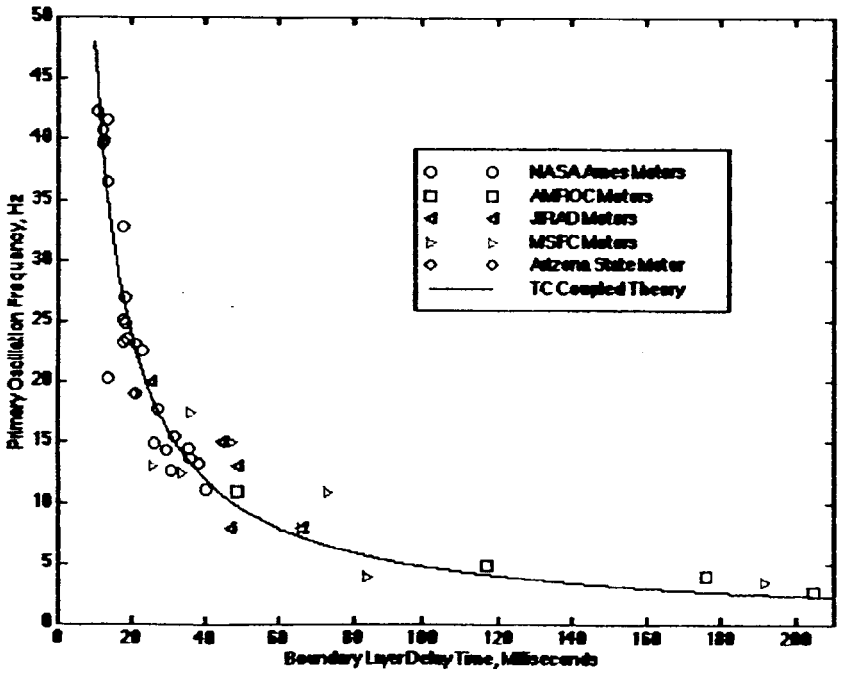

Figure 12: Comparison of the TCG coupled oscillation frequency prediction with the hybrid motor test data available in the literature.

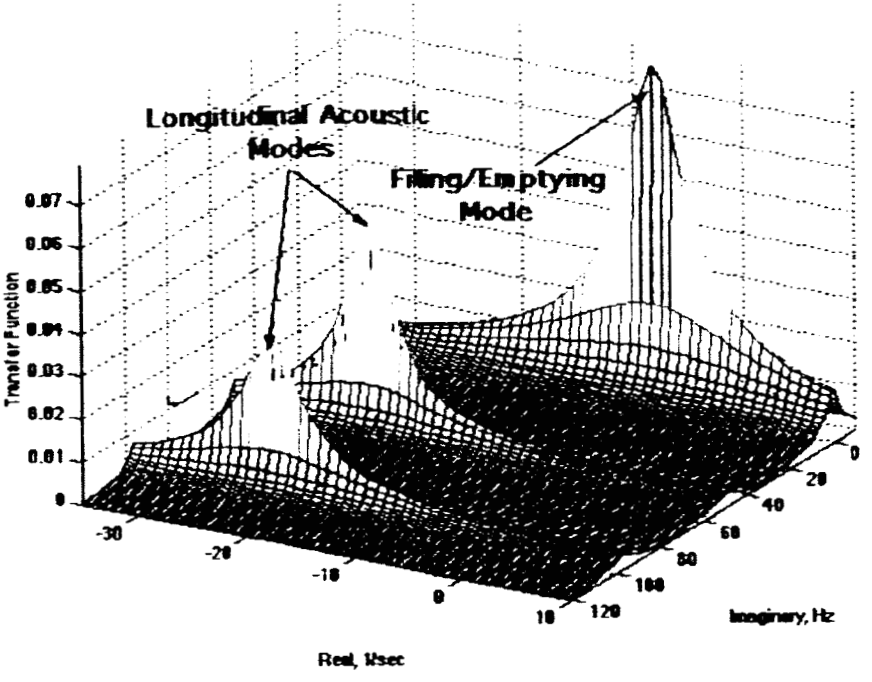

Figure 13: The plot of the transfer function for the pure gas dynamic system.

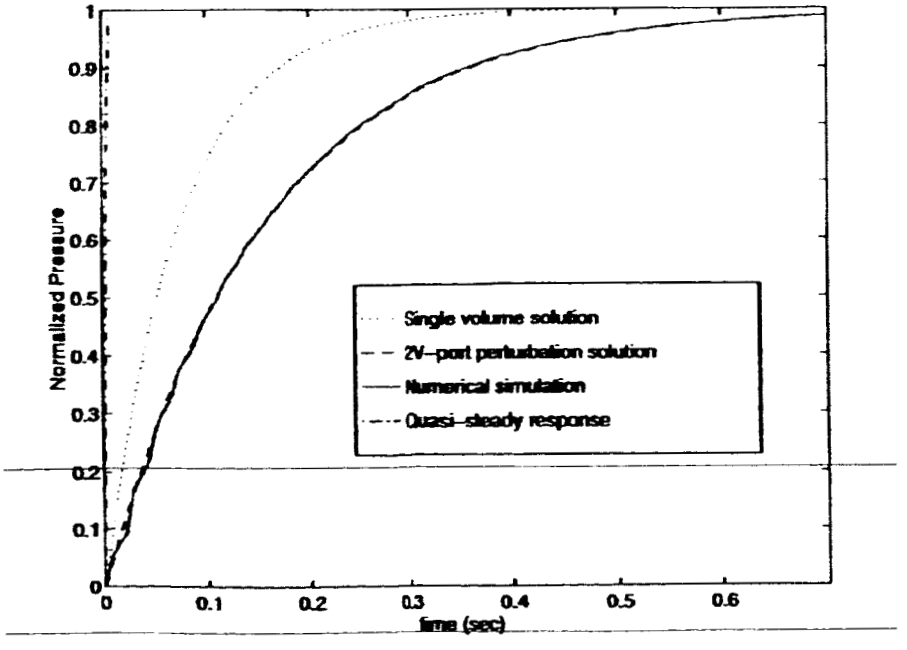

Figure 14: The throttling response for the pure gas dynamic system.

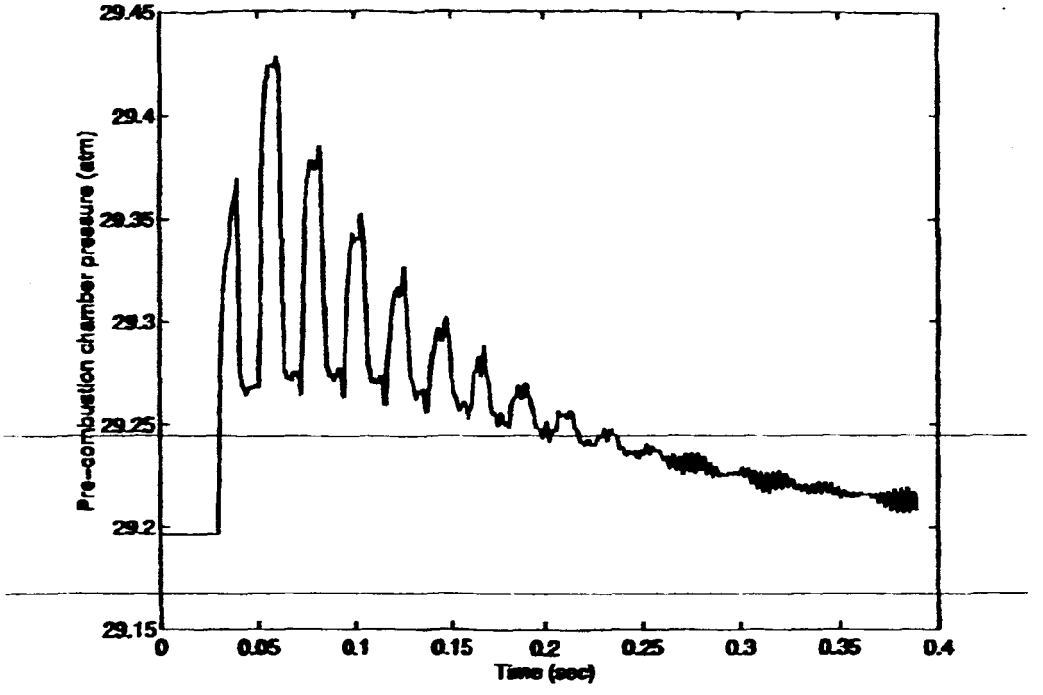

Figure 15: The response of the pre-combustion chamber pressure to a disturbance of the oxidizer mass flow rate.